MNRAS **000**, 1–14 (2019) Preprint 9 February 2022 Compiled using MNRAS LATEX style file v3.0

The afterglow and kilonova of the short GRB 160821B

E. Troja[1,2⋆], A. J. Castro-Tirado[3,4], J. Becerra González[5,6], Y. Hu[3,7], G. S. Ryan[1,8], S. B. Cenko[2,1,8], R. Ricci[9], G. Novara[10], R. Sánchez-Rámirez[11], J. A. Acosta-Pulido[6,5], K. D. Ackley[12] M. D. Caballero García[13], S. S. Eikenberry[12], S. Guziy[14], S. Jeong[15], A. Y. Lien[2], I. Márquez[3], S. B. Pandey[16], I. H. Park[15], T. Sakamoto[17], J. C. Tello[13], I. V. Sokolov[18], V. V. Sokolov[19], A. Tiengo[9,20,21], A. F. Valeev[19], B. B. Zhang[22,23], S. Veilleux[1,8]

[1] *Department of Astronomy, University of Maryland, College Park, MD 20742-4111, USA*
[2] *Astrophysics Science Division, NASA Goddard Space Flight Center, 8800 Greenbelt Rd, Greenbelt, MD 20771, USA*
[3] *Instituto de Astrofísica de Andalucia (IAA-CSIC), Glorieta de la Astronomia sn, E-18008, Granada, Spain*
[4] *Unidad Asociada Departamento de Ingeniería de Sistemas y Automática, E.T.S. de Ingenieros Industriales, Universidad de Málaga, Spain*
[5] *Universidad de La Laguna, Dpto. Astrofísica, E-38206 La Laguna, Tenerife, Spain*
[6] *Instituto de Astrofísica de Canarias, E-38200 La Laguna, Tenerife, Spain*
[7] *Universidad de Granada, Facultad de Ciencias Campus Fuentenueva S/N CP 18071 Granada, Spain*
[8] *Joint Space Science Institute, University of Maryland, College Park, MD 20742-4111, USA*
[9] *INAF-Istituto di Radioastronomia, Via Gobetti 101, I-40129, Italy*
[10] *Scuola Universitaria Superiore IUSS Pavia, Piazza della Vittoria 15, I-27100 Pavia, Italy*
[11] *INAF, Istituto di Astrofisica e Planetologia Spaziali, via Fosso del Cavaliere 100, 00133 Rome, Italy*
[12] *Department of Astronomy, University of Florida, Gainesville, FL 32611*
[13] *Astronomical Institute of the Academy of Sciences, Boční II 1401, CZ-14100 Praha 4, Czech Republic*
[14] *Nikolaev National University, Nikolska 24, Nikolaev 54030, Ukraine*
[15] *Institute for Science and Technology in Space, SungKyunKwan University, Suwon 16419, Korea*
[16] *Aryabhatta Research Institute of Observational Sciences, Manora Peak, Nainital - 263 002, India*
[17] *Department of Physics and Mathematics, Aoyama Gakuin University, 5-10-1 Fuchinobe, Chuoku, Sagamiharashi Kanagawa 252-5258, Japan*
[18] *Terskol Branch of Institute of Astronomy of the RAS, 48 Pyatnitskaya st., Moscow, 119017 Russia*
[19] *Special Astrophysical Observatory of RAS, Nizhniy Arkhyz, Zelenchukskiy region, Karachai-Cherkessian Republic, 369167, Russia*
[20] *INAF, Istituto di Astrofisica Spaziale e Fisica Cosmica Milano, Via E. Bassini 15, I-20133 Milano, Italy*
[21] *INFN-Istituto Nazionale di Fisica Nucleare, Sezione di Pavia, via A. Bassi 6, I-27100 Pavia, Italy*
[22] *School of Astronomy and Space Science, Nanjing University, 163 Xian-Lin Ave., Nanjing 210023, China*
[23] *Key Laboratory of Modern Astronomy and Astrophysics (Nanjing University), Ministry of Education, China*

Accepted 2019 Aug 12. Received 2019 Aug 12; in original form 2019 May 3

ABSTRACT

GRB 160821B is a short duration gamma-ray burst (GRB) detected and localized by the *Neil Gehrels Swift Observatory* in the outskirts of a spiral galaxy at z=0.1613, at a projected physical offset of ≈16 kpc from the galaxy's center. We present X-ray, optical/nIR and radio observations of its counterpart and model them with two distinct components of emission: a standard afterglow, arising from the interaction of the relativistic jet with the surrounding medium, and a kilonova, powered by the radioactive decay of the sub-relativistic ejecta. Broadband modeling of the afterglow data reveals a weak reverse shock propagating backward into the jet, and a likely jet-break at ≈3.5 d. This is consistent with a structured jet seen slightly off-axis ($\theta_{view} \sim \theta_{core}$) while expanding into a low-density medium ($n \approx 10^{-3}$ cm^{-3}). Analysis of the kilonova properties suggests a rapid evolution toward red colors, similar to AT2017gfo, and a low nIR luminosity, possibly due to the presence of a long-lived neutron star. The global properties of the environment, the inferred low mass ($M_{ej} \lesssim 0.006\ M_{\odot}$) and velocities ($v_{ej} \gtrsim 0.05c$) of lanthanide-rich ejecta are consistent with a binary neutron star merger progenitor.

Key words: gamma-ray burst: general – nuclear reactions, nucleosynthesis, abundances – stars: neutron – gravitational waves

1 INTRODUCTION

Short duration GRBs were long suspected to be the product of compact binary mergers (Blinnikov et al. 1984; Goodman 1986; Paczynski 1986; Eichler et al. 1989; Narayan et al. 1992), involving either two neutron stars (NSs) or a NS and a solar-mass black hole (BH). The merger remnant, either a massive NS (Bucciantini et al. 2012; Giacomazzo & Perna 2013) or an accreting BH (Ruffert & Janka 1999; Baiotti et al. 2008; Kiuchi et al. 2009), launches a highly relativistic jet, which produces the GRB emission (Rezzolla et al. 2011; Paschalidis, Ruiz & Shapiro 2015; Ruiz et al. 2016). Later, the interaction of this jet with the surrounding medium produces the observed broadband (from radio to X-rays) afterglow spectrum via synchrotron radiation (e.g. Granot & Sari 2002). Within this framework, the study of the GRB afterglow probes the jet structure and geometry as well as the properties of the surrounding environment.

Another long-standing prediction of the NS merger model is the presence of a luminous, short-lived transient arising from the radioactive decay of freshly synthesized r-process elements (Li & Paczyński 1998; Metzger et al. 2010; Barnes & Kasen 2013; Tanaka & Hotokezaka 2013). Whereas the afterglow does not provide any direct link to the GRB progenitor, such radioactively powered transient, initially dubbed "mini-supernova" and now more commonly referred to as "kilonova", is the distinctive signature of compact binary mergers and clear signpost of heavy elements production in these systems (Lattimer & Schramm 1974, 1976; Freiburghaus et al. 1999; Roberts et al. 2011; Goriely et al. 2011; Korobkin et al. 2012; Grossman et al. 2014; Rosswog et al. 2014). Evidence of kilonovae associated to short GRBs was only recently found (Tanvir et al. 2013; Yang et al. 2015; Jin et al. 2016). The timescales and red color of these first candidate kilonovae suggested that the merger ejecta were highly opaque, as predicted for the heaviest r-process elements (Barnes & Kasen 2013; Tanaka & Hotokezaka 2013). The high opacity causes any UV/optical emission to be significantly suppressed, thus naturally explaining the lack of kilonova detections in over a decade of *Swift* observations (Bloom et al. 2006; Kocevski et al. 2010; Kann et al. 2011; Pandey et al. 2019).

This slowly-progressing field was revolutionized by the discovery of GW170817 and its electromagnetic counterparts (Abbott et al. 2017a; Abbott et al. 2017b). X-ray observations revealed the onset of an off-axis afterglow (Troja et al. 2017) powered by a relativistic structured jet (Mooley et al. 2018; Ghirlanda, et al. 2019; Troja et al. 2019). Thanks to the proximity of the event, the associated kilonova AT2017gfo was characterized in great detail (e.g. Covino, et al. 2017; Pian et al. 2017; Smartt et al. 2017; Tanvir et al. 2017; Troja et al. 2017). In addition to the expected red emission, peaking in the nIR a few days after the merger, a distinctive feature of AT2017gfo was its luminous UV/optical light, peaking at early times and rapidly fading away (Evans et al. 2017). Although the origin of this blue component remains an open question, it immediately revealed a complex chemical composition and velocity structure of the merger ejecta, indicating that the phenomenology of a kilonova is likely determined by the interplay of multiple outflows emerging from the merger remnant (Kasen et al. 2017; Perego et al. 2017; Radice et al. 2018; Wollaeger et al. 2018).

Fostered by the discovery of AT2017gfo and its luminous blue emission, several attempts were made to find similar cases in archival short GRB observations (Gompertz et al. 2018; Troja et al. 2018b; Rossi et al. 2019). Troja et al. (2018b) found that some nearby events have optical luminosities comparable to AT2017gfo. In particular, they showed that the short GRB150101B was a likely analogue to GW170817, characterized by a late-peaking afterglow and a luminous optical kilonova emission, dominating at early times. Other, although less clear, cases discussed in the literature include GRB060505 (Ofek et al. 2007) and GRB080503 (Perley et al. 2009). Overall, it seems plausible that kilonovae similar to AT2017gfo could have been detected in the optical, although not clearly identified prior to GW170817.

Whereas this observational evidence suggests that r-process nucleosynthesis is common in the aftermath of a short GRB, it does not inform on the production of the heaviest elements, i.e. those with atomic mass number $A \gtrsim 140$. NS merger ejecta with an electron fraction $Y_e \gtrsim 0.25$ do not have enough neutrons to push the nuclear chain past the second r-process peak at $A \approx 130$, thus producing only a blue and fast-fading kilonova (Li & Paczyński 1998; Metzger et al. 2010). An efficient production of lanthanides and actinides will increase the ejecta opacity, leading to a delayed and redder kilonova emission (Barnes & Kasen 2013; Tanaka & Hotokezaka 2013). Only the detection of such red component, peaking at IR wavelengths, is a clear signature of the production of heavy ($A \gtrsim 140$) r-process nuclei. Unfortunately, archival IR observations of short GRBs are sparse and mostly unconstraining, and the only possible nIR detection of a kilonova in a short GRB remains GRB130603B (Tanvir et al. 2013).

The short duration GRB160821B, thanks to its low redshift and a rich multi-wavelength dataset, is an excellent testbed for kilonova searches and afterglow studies. The presence of a kilonova was discussed by Kasliwal et al. (2017a) and Jin et al. (2018), who did not find conclusive evidence for it due to the sparse dataset used in both studies. Here we present a comprehensive broadband analysis of this event, including data from *Swift* and *XMM-Newton* in the X-rays, the Gran Telescopio de Canarias (GTC), the William Herschel Telescope (WHT), the *Hubble Space Telescope* (HST), the Keck I telescope, and the Discovery Channel Telescope (DCT) in the optical/nIR, and the Jansky Very Large Array (VLA) in the radio. Thanks to the good temporal and spectral coverage of our dataset, we resolve two emission components, which we identify as the GRB afterglow and its associated kilonova. We can exclude dust as the origin of the observed red color, and interpret it as evidence for a lanthanide-rich kilonova emission.

Throughout the paper, we adopt a standard ΛCDM cosmology (Planck Collaboration et al. 2018). Unless otherwise stated, the quoted errors are at the 68% confidence level, and upper limits are at the 3 σ confidence level.

2 OBSERVATIONS AND DATA ANALYSIS

GRB 160821B triggered the *Swift* Burst Alert Telescope (BAT; Barthelmy et al. 2005) at 22:29:13 UT on 2016 August 21, hereafter referred to as T_0. Based on its duration of T_{90} =0.48±0.07 s (Lien et al. 2016), it is classified as a short burst. According to the BAT GRB catalogue[1], its spectrum is relatively soft, and best described (χ^2=59 for 59 dof) by a power-law with a high-energy exponential cut-off at ≈50 keV. The time-averaged fluence is $(1.10 \pm 0.10) \times 10^{-7}$ erg cm^{-2} s^{-1} in the 15-150 keV energy band. The Fermi GBM Burst catalogue[2] reports a fluence of $(2.0 \pm 0.2) \times 10^{-7}$ erg cm^{-2} s^{-1} over the broader the 10-1,000 keV energy band. Using this value and the redshift $z \sim 0.1613$ from the candidate host galaxy (see Sect. 2.2.6), we derive an isotropic-equivalent energy $E_{\gamma,iso} = (1.3 \pm 0.3) \times 10^{49}$ erg in the 10-1,000 keV energy band, at the lower end of the observed distribution of short GRB energetics.

Its short duration and possible low redshift made it a prime target for kilonova searches, triggering an intense multi-wavelength campaign, as we describe in detail below. A log of the observations is reported in Table 1.

2.1 X-rays

2.1.1 Swift/XRT

Observations with the X-Ray Telescope (XRT; Burrows et al. 2005) on-board *Swift* started 57 s after the trigger, and monitored the afterglow for the following 23 days for a total net exposure of 198 s in Windowed Timing (WT) mode and 39 ks in Photon Counting (PC) mode. *Swift* data were retrieved from the public on-line repository[3] (Evans et al. 2009) by using custom options for the light curve binning and standard settings for the spectral extraction. Spectra were modelled within XSPEC v.12.10.1 (Arnaud 1996) by minimizing the Cash statistics (Cash 1979). The Galactic absorption column was modelled with the function `tbabs` and fixed to the value $N_{\rm H} = 5.7 \times 10^{20}$ cm^{-2} (Willingale et al. 2013). The time-averaged spectrum, from 4 ks to 74 ks, is well described by an absorbed power-law function with photon index $\Gamma = 1.8 \pm 0.2$. Based on this model, we derive a counts-to-unabsorbed flux conversion factor of 4.4×10^{-11} erg cm^{-2} ct^{-1}. The derived X-ray fluxes are reported in Table 1. No evidence for intrinsic absorption was found at the galaxy's redshift of $z \sim 0.1613$, and we place a $3\,\sigma$ upper limit $N_{{\rm H},z} < 5.5 \times 10^{21}$ cm^{-2} using the model `ztbabs`.

2.1.2 XMM-Newton

The X-ray afterglow was also observed with *XMM-Newton* at two epochs, on 2016 August 25 (obsID: 0784460301) and on 2016 August 31 (obsID: 0784460401; PI: Tanvir). The PN (Strüder et al. 2001) and two MOS (Turner et al. 2001) CCD cameras operated in Full Frame mode and with the thin optical blocking filter. The PN, MOS1 and MOS2 exposure times were, respectively: 24.6 ks, 27.1 ks, 27.1 ks for the first observation and 34.1 ks, 36.0 ks, 35.9 ks for the second observation.

Data were retrieved from the public archive, and processed using the XMM-Newton Science Analysis Software (SAS; Gabriel et al. 2004) version 16.1.0. After removing intervals of high particle background, the effective exposures were reduced by ≈55% for the first observation and ≈30% for the second observation. For our analysis we selected only events with FLAG=0 and PATTERN≤4 and PATTERN≤12 for PN and MOS, respectively.

The afterglow is detected with high significance during the first *XMM* epoch. Source spectra were extracted from a circular region with radius of 20″, and the background was estimated from two independent source-free boxes around the afterglow position. We extracted 57 source counts from the PN exposure, and modeled the spectrum as described in Sect. 2.1.1 with an absorbed power-law function of photon index $\Gamma = 1.88 \pm 0.24$. During the second epoch, the source is still visible with a detection likelihood (DET_ML=7.9) slightly above the standard detection threshold adopted for the *XMM-Newton* source catalogues (DET_ML=6). By summing PN and MOS data, we extract a total of 47 source counts. The corresponding X-ray flux was derived by assuming the same spectral parameters of the first epoch. Our results are reported in Table 1.

2.2 Optical/nIR

2.2.1 Swift/UVOT

Observations with the Ultra-Violet Optical Telescope (UVOT; Roming et al. 2006) on-board *Swift* started 76 s after the trigger. The GRB position was initially imaged with the *white* and *u* filters, but no counterpart was detected. We used the zero-points provided by Breeveld et al. (2011) to convert UVOT count rates into the AB magnitude system (Oke 1974). The corresponding $3\,\sigma$ upper limits are reported in Table 1. Subsequent observations used all the optical and UV filters, and are reported in Breeveld & Siegel (2016).

2.2.2 Gran Telescopio Canarias (GTC)

We observed the GRB afterglow (PI: A. Castro-Tirado) with the 10.4 m Gran Telescopio de Canarias (GTC), located at the observatory of Roque de los Muchachos in La Palma (Canary Islands, Spain), equipped with the Optical System for Imaging and low-intermediate-Resolution Integrated Spectroscopy (OSIRIS) and the Canarias InfraRed Camera Experiment (CIRCE) instruments. Deep optical images in the g, r, i, and z filters were taken over five different nights, starting as early as 1.8 hr after the trigger, in order to characterize any spectral evolution of the GRB counterpart (Xu et al. 2016). A single epoch of nIR imaging in the J, H, and K_s filters was carried out ≈2 d after the trigger.

Data were reduced and aligned in a standard fashion using a custom pipeline, based mainly on *Astropy* and *photutils* python libraries. We combined the images by weighting each individual frame based on its depth, and applying a 3σ clipping algorithm. Photometric zero points and astrometric calibration were computed using the Pan-STARRS catalogue (Chambers, et al. 2016). We then performed point spread function (PSF) matching photometry of the afterglow

[1] https://swift.gsfc.nasa.gov/results/batgrbcat/
[2] https://heasarc.gsfc.nasa.gov/W3Browse/fermi/fermigbrst.html
[3] http://www.swift.ac.uk/xrt_products/

Table 1. Observations of GRB160821B.

Date MJD	T-T_0 (d)	Telescope	Instrument	Exposure (s)	Band	AB mag	Flux density[4] (μJy)
			Optical/nIR				
57621.940	0.002	*Swift*	UVOT	147	wh	>21.9	<8
57621.942	0.004	*Swift*	UVOT	209	u	>21.4	<12
57622.013	0.076	GTC	OSIRIS	270	r	22.67±0.10	3.4±0.3
57622.017	0.080	GTC	OSIRIS	270	i	22.39±0.07	4.3±0.3
57622.020	0.083	GTC	OSIRIS	180	z	22.28±0.06	4.7±0.3
57623.006	1.07	WHT	ACAM	1440	r	23.83±0.25	1.2±0.3
57623.027	1.09	WHT	ACAM	1680	z	23.6±0.3	1.4±0.4
57623.878	1.941	GTC	CIRCE	540	H	>23.8	<1.1
57623.895	1.958	GTC	CIRCE	1800	J	>24.0	<0.9
57623.921	1.984	GTC	CIRCE	600	K_s	>23.3	<1.7
57623.958	2.021	GTC	OSIRIS	800	g	25.67±0.15	0.22±0.03
57623.965	2.028	GTC	OSIRIS	720	r	25.12±0.12	0.36±0.04
57623.973	2.036	GTC	OSIRIS	450	i	24.56±0.12	0.58±0.06
57623.980	2.043	GTC	OSIRIS	420	z	24.31±0.17	0.72±0.11
57625.564	3.627	HST	WFC3	2484	$F606W$	26.02±0.06	0.157±0.009
57625.631	3.694	HST	WFC3	2397	$F160W$	24.53±0.08	0.57±0.04
57625.697	3.760	HST	WFC3	2397	$F110W$	24.82±0.05	0.44±0.02
57625.929	3.992	GTC	OSIRIS	450	g	>25.6	<0.24
57625.934	3.997	GTC	OSIRIS	420	i	>25.8	<0.19
57626.234	4.297	Keck I	MOSFIRE	160	K_s	24.0±0.4	0.9±0.3
57626.922	4.985	GTC	OSIRIS	800	r	26.49±0.20	0.101±0.019
57629.402	7.465	Keck I	MOSFIRE	145	K_s	>23.9	<0.9
57630.321	8.383	Keck I	MOSFIRE	110	K_s	>23.7	<1.2
57631.924	9.987	GTC	OSIRIS	720	i	>26.0	<0.15
57631.935	9.998	GTC	OSIRIS	1200	g	>25.8	<0.20
57631.950	10.013	GTC	OSIRIS	960	r	>26.2	<0.13
57632.325	10.388	HST	WFC3	1863	$F606W$	27.9±0.3	0.028±0.008
57632.383	10.446	HST	WFC3	2397	$F110W$	26.9±0.4	0.07±0.02
57632.449	10.512	HST	WFC3	2397	$F160W$	26.6±0.3	0.08±0.02
57645.088	23.151	HST	WFC3	1350	$F606W$	>27.2	<0.05
57645.108	23.171	HST	WFC3	1497	$F110W$	>26.6	<0.09
57645.154	23.217	HST	WFC3	2097	$F160W$	>25.7	<0.19
57721.2	99.2	HST	WFC3	5395	$F110W$	reference	–
57725.3	103.3	HST	WFC3	2484	$F606W$	reference	–
58333.7	711.7	HST	WFC3	2796	$F160W$	reference	–
			Radio				
57622.11	0.17	VLA	–	3600	C	–	26 ± 5
57623.06	1.13	VLA	–	3600	C	–	< 15
57632.01	10.07	VLA	–	6480	X	–	< 11
57639.04	17.10	VLA	–	6460	X	–	< 33
			X-ray				
57721.995	0.057	*Swift*	XRT	185	0.3 – 10 keV	–	$0.15^{+0.08}_{-0.06}$
57722.001	0.063	*Swift*	XRT	566	0.3 – 10 keV	–	$0.05^{+0.03}_{-0.02}$
57722.008	0.070	*Swift*	XRT	784	0.3 – 10 keV	–	0.05±0.02
57722.064	0.126	*Swift*	XRT	363	0.3 – 10 keV	–	$0.08^{+0.04}_{-0.03}$
57722.068	0.130	*Swift*	XRT	396	0.3 – 10 keV	–	$0.07^{+0.04}_{-0.03}$
57722.074	0.136	*Swift*	XRT	865	0.3 – 10 keV	–	$0.037^{+0.018}_{-0.014}$
57722.132	0.195	*Swift*	XRT	862	0.3 – 10 keV	–	0.035±0.019
57722.222	0.285	*Swift*	XRT	1273	0.3 – 10 keV	–	$0.025^{+0.014}_{-0.010}$
57722.264	0.327	*Swift*	XRT	584	0.3 – 10 keV	–	0.05±0.02
57722.278	0.340	*Swift*	XRT	1584	0.3 – 10 keV	–	0.029±0.011
57722.356	0.419	*Swift*	XRT	3908	0.3 – 10 keV	–	0.014±0.05
57722.962	1.024	*Swift*	XRT	9008	0.3 – 10 keV	–	$(3.6\pm0.2)\times10^{-3}$
57724.725	2.327	*Swift*	XRT	8777	0.3 – 10 keV	–	$<4.6\times10^{-3}$
57625.879	3.942	XMM-Newton	EPIC/PN	10880	0.3 – 10 keV	–	$(2.3\pm0.3)\times10^{-3}$
57631.913	9.976	XMM-Newton	EPIC/PN	22665	0.3 – 10 keV	–	$(2.9\pm1.5)\times10^{-4}$
57737.570	15.172	*Swift*	XRT	26000	0.3 – 10 keV	–	$<10^{-3}$

[3] Optical/nIR fluxes were corrected for Galactic extinction due to the reddening $E(B-V)$ =0.04 along the sightline (Green et al. 2018). X-ray fluxes were corrected for Galactic absorption N_H=5.7×10^{20} cm^{-2} (Willingale et al. 2013), and converted into flux densities at 1 keV using the best fit photon index Γ=1.88.

on the combined images. To construct the empirical PSF, we selected bright and isolated stars close to the afterglow, and combined them weighting by their flux. Background and host light contamination were left as free parameters in the fit. The resulting values are reported in Table 1.

On August 23 ($\approx T_0$+2 d), a GTC (+OSIRIS) spectrum (3 × 1500s) with the R1000B grism and a 1.″slit covering the 3,700,Å-7,500, Å range was gathered with the slit being placed in order to cover the GRB location. Data were reduced and calibrated using standard routines. No absorption or emission lines can be detected superimposed on the continuum emission.

2.2.3 *William Herschel Telescope (WHT)*

Optical imaging with the Auxiliary port CAMera (ACAM) started on 2016-08-22 at 23:55 ($\approx T_0$ + 1.1 d; Levan et al. 2016). Observations were carried out in the r filter for a total integration of 24 min and in z filter for a total exposure of 28 min. Seeing during the observations was around 0.8″. The data were reduced within IRAF[5] following standard procedures (e.g., bias subtraction, flat-fielding, etc.). Aperture photometry was performed using the *photutils*[6] package, and calibrated to nearby Pan-STARRS sources (Chambers, et al. 2016). A 20% systematic uncertainty was added to our measurements to account for contaminating light from the nearby candidate host galaxy. Our measurements are reported in Table 1.

2.2.4 *Hubble Space Telescope (HST)*

We activated our program to search for kilonovae (GO14087,GO14607; PI: Troja) and, starting on August 22, obtained several epochs of deep imaging with the IR and UVIS channels of the Wide Field Camera 3 (WFC3). A complete log of the observations is reported in Table 1. Data were processed through the STSCI pipeline, and standard tools within the *stsci_python* package on AstroConda[7] were used to align, drizzle and combine the exposures into the final images. The resulting plate scales were 0.067″/pixel for the WFC3/IR images and 0.033″/pixel for the WFC3 F606W images. Late-time observations of the host galaxy were used as reference templates. Aperture photometry was performed on the subtracted images, and the tabulated zero points were used to to determine the source brightness.

The GRB counterpart is detected in all filters in the earlier two epochs, whereas is no longer visible in subsequent visits. Its position, determined from the optical frames, is R.A. (J2000) = 18:39:54.56, Dec (J2000) = +62:23:30.35 with a 1 σ uncertainty of 0.04″, and lies 5.7″ from the center of a bright face-on spiral (Figure 1, which is likely the GRB host galaxy. At a redshift z∼0.1613, this corresponds to a projected physical offset of 16.40±0.12 kpc.

2.2.5 *Keck*

NIR observations with the MOSFIRE instrument on the Keck I telescope were taken at three different epochs, as previously reported by Kasliwal et al. (2017a). A possible detection was found during the first epoch at T_0+4.3 d, whereas the source was undetected at later times. We retrieved the archival data, and independently analyzed them using standard procedures for CCD data reduction. For the first epoch, four frames considered particularly noisy were removed, whereas the remaining ones were aligned using SCAMP (Bertin 2006) and stacked with SWarp (Bertin et al. 2002) into a final image with 160 s of total exposure. Our analysis confirms the presence of a weak signal ($\approx$3.5 σ) at the GRB position. A magnitude of K_s=22.12±0.38 was derived by performing aperture photometry calibrated to nearby point sources from the Two Micron All Sky Survey (2MASS; Skrutskie et al. 2006). Our result is in agreement with the value quoted by Kasliwal et al. (2017a). We used the offsets from Blanton & Roweis (2007) to convert the 2MASS Vega magnitudes to the AB system, as quoted in Table 1.

2.2.6 *Discovery Channel Telescope (DCT)*

The DeVeny spectrograph on the 4.3-meter DCT was used on 2017 March 19 with the 300 g mm^{-1} grating in the first order and a 1.″5 slit to obtain a spectrum for the GRB host galaxy, covering the 3,600,Å- 8,000 Å range at a dispersion of ∼2.2 Å per pixel. Standard IRAF procedures were used for reduction and calibration.

The final spectrum is shown in Figure 1 (bottom panel). Several nebular emission lines are visible, including those at $\lambda_{obs} \approx$ 4329, 5814, 5759, and 5647 Å, associated with [O II], $H\beta$ and [O III] transitions, respectively, and identify the galaxy to be at z = 0.1613±0.0004, consistent with the preliminary estimate of Levan et al. (2016). The bright line at 7622 Å, associated with the Balmer $H\alpha$ line, falls within the telluric A band. Lines properties were derived by modeling them with Gaussian functions using the *splot* task in IRAF.

2.3 Radio

Radio observations were carried out with the Karl J. Jansky Very Large Array (JVLA) at four different epochs, on Aug 22 and 23, 2016 (project code: 15A-235; PI: Fong), and on Sep 1 and 8, 2016 (project code: 16B-386; PI: Gompertz) in B configuration at the center frequencies of 6 GHz with a bandwidth of 2 GHz (the former two epochs) and 10 GHz with a bandwidth of 4 GHz (the latter two epochs). The primary calibrator was 3C286 and the phase calibrator was J1849+6705 for all the four epochs. The data were downloaded from the VLA Archive and calibrated using the JVLA CASA pipeline v1.3.11 running in CASA v4.7.2. The data were then split, imaged and cleaned using CASA in interactive mode: Briggs weighting, robustness = 0.5 and 1000 clean iterations were performed. The results are presented in Table 1. The afterglow was detected during the first epoch at a flux of ≈26 μJy, consistent within the uncertainties with

[5] IRAF is distributed by the National Optical Astronomy Observatory, which is operated by the Association of Universities for Research in Astronomy (AURA) under cooperative agreement with the National Science Foundation.
[6] https://photutils.readthedocs.io/en/stable/
[7] AstroConda is a free Conda channel maintained by the Space Telescope Science Institute (STScI). It provides tools and utilities required to process and analyse data from the Hubble Space Telescope (HST), James Webb Space Telescope (JWST), and others: http://AstroConda.readthedocs.io/

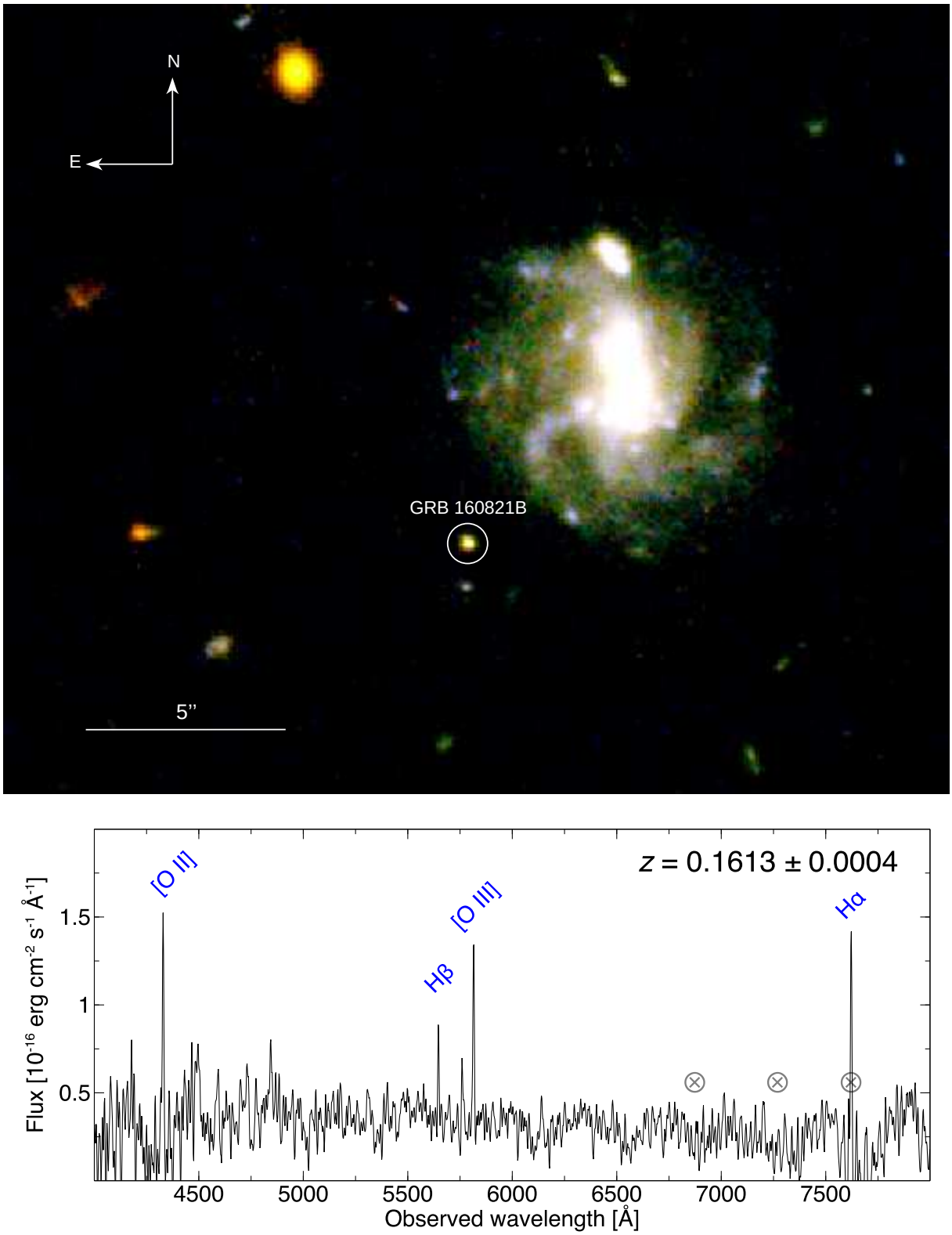

Figure 1. *Top panel:* the field of GRB160821B observed with HST using the $F606W$ (blue), $F110W$ (green), and $F160W$ (red) filters. The white circle marks the position of the GRB counterpart, located ≈16 kpc from the center of its galaxy. *Bottom panel:* optical spectrum of the GRB host galaxy taken with the DeVeny spectrograph on the 4.3m DCT. The brightest lines are identified. The crossed circles mark the position of strong telluric features.

the value reported in Fong et al. (2016). By performing a 2D Gaussian fit to the source region we obtain a position of R.A. (J2000) = 18:39:54.56, Dec (J2000) = 62:23:30.32 with an error of 0.07 arcsec and 0.08 arcsec, respectively. This is consistent with the optical position (Sect. 2.2.4). For the other epochs a 3 σ flux density upper limit is provided.

3 DISENTANGLING THE AFTERGLOW AND KILONOVA EMISSION

The kilonova AT2017gfo was characterized by a quasi-thermal spectrum peaking in the optical/UV and rapidly evolving toward redder wavelengths (e.g. Pian et al. 2017; Drout et al. 2017), in overall agreement with kilonova models (e.g. Kasen et al. 2017; Kasen et al. 2015). The color evolution of GRB 160821B (Figure 2) is consistent with a similar behavior. By using a simple power-law model, $F_\nu \propto^{-\beta}$ to describe the data, we derive β=0.70±0.20 at T_0+2 hr, rather standard for an afterglow spectrum with $\nu_m < \nu < \nu_c$ (Granot & Sari 2002). Data from the first night of observations show a flatter spectrum, $\beta \approx$0.30, although with larger uncertainties. The optical/nIR counterpart displays a much redder color, $\beta \approx$1.4–1.8, between 2 and 4 days, and then return to a more typical value of β=1.1±0.30. Evidence of a possible spectral break at $\lambda \approx$10,000 Å is seen in the GTC OSIRIS and CIRCE data at T_0+2 d, but no longer visible at later times. Whereas spectral breaks are observed in many GRB afterglows, the change in spectral slope $\Delta\beta \gtrsim$1.0 implied by our observation is hard to reconcile with standard afterglow theory. Substantial color variation is often observed during the early ($\lesssim 10^3$ s) afterglow phases (e.g. Melandri, et al. 2017), but is uncommon on longer timescales (Li, et al. 2018). The observed color evolution in GRB 160821B appears atypical for a GRB afterglow, and instead consistent with the onset of a kilonova peaking in the optical at $\lesssim$1 d, then rapidly shifting to longer wavelengths. In our last observation, the intermediate value of the spectral index suggests a significant contribution from the underlying afterglow. This implies that the IR emission started to fade a few days after the burst, as observed in AT2017gfo, and is therefore shorter lived than the candidate kilonova component in GRB130603B (Tanvir et al. 2013).

No significant emission from the kilonova AT2017gfo was detected at X-ray or radio wavelengths (Troja et al. 2017; Hallinan et al. 2017). Based on this evidence, we use the X-ray and radio emission to trace the underlying afterglow component, and compare it to the optical/nIR dataset in order to detect any excess from the kilonova. In order to model the afterglow, we consider a standard scenario (e. g. Zhang & Mészáros 2004, and references therein) in which the interaction between the jet and the environment generates two shocks: a highly relativistic forward shock (FS) propagating into the outer medium, and a mildly relativistic reverse shock (RS) traveling backward into the ejecta. The shocked electrons are accelerated into a power-law distribution, $N(E) \propto E^{-p}$, and emit their energy via synchrotron radiation. The resulting broadband spectrum is characterized by four quantities: the self-absorption frequency ν_a, the synchrotron frequency ν_m, the cooling frequency ν_c and the peak flux F_{pk}, where we use the subscript FS and RS to distinguish the two spectral components.

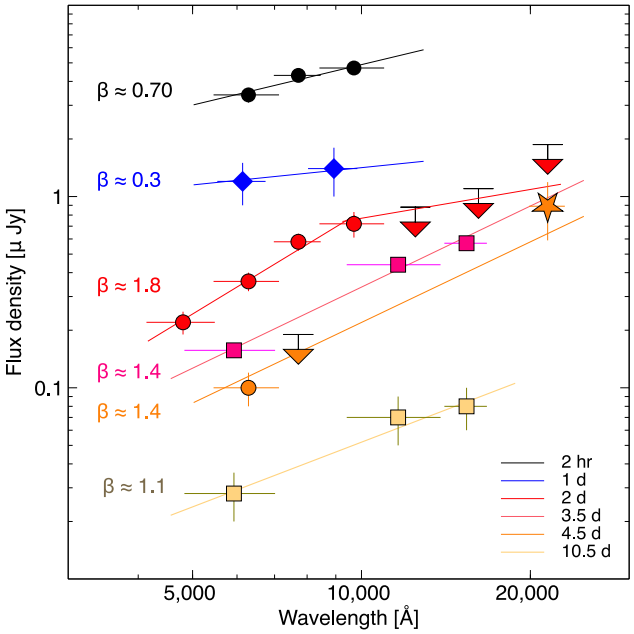

Figure 2. Color evolution of the optical/nIR counterpart, compiled including data from GTC (circles), WHT (diamonds), Keck (star), and HST (squares).

Template light curves for the kilonova emission were synthesized by interpolating over the rest-frame spectra of AT2017gfo, and stretching times by a factor of $(1 + z)$. We used the spectroscopic data from VLT/X-Shooter (Pian et al. 2017; Smartt et al. 2017) and *HST* (Troja et al. 2017) for t>1.5 d, and photometric measurements from Drout et al. (2017); Evans et al. (2017); Tanvir et al. (2017); Troja et al. (2017) at earlier times.

3.1 Basic Constraints to the Afterglow

The early X-ray afterglow displays a bright and rapidly fading light curve (Figure 3). The measured X-ray flux decreases from 2×10^{-10} erg cm^{-2} s^{-1} at 250 s post-burst to 2×10^{-12} erg cm^{-2} s^{-1} at 400 s, implying a temporal slope $\alpha \approx$9, where $F_X \propto t^{-\alpha}$. This sharp decay cannot be reproduced by standard FS models and is generally attributed to the sudden cessation of central engine activity (Troja et al. 2007; Rowlinson et al. 2010). Other scenarios, invoking a bright RS emission (e.g. Uhm & Beloborodov 2007; van Eerten 2014), are not consistent with the simultaneous optical upper limits, nor with the constraints from the radio afterglow data (see below). We therefore attribute this first phase of the afterglow to the continuous activity of the central engine (see also Lü et al., 2017), and exclude it from subsequent modeling.

After the first orbit, the X-ray afterglow follows a simple power-law decay with slope $\alpha_1 = 0.84\pm0.08$. The condition $\beta_X \gtrsim \beta_{\rm opt} \approx 0.7$ is satisfied for an electron spectral index $p \approx 2.3$ when the cooling frequency ν_c^{FS} lies within or above the X-ray band. Given its slow temporal evolution, $\nu_c \propto t^{-0.5}$, its passage does not affect the optical/nIR data over the time span of our observations. This additional evidence adds support to the idea that the observed color evolution is not related to the GRB afterglow. A comparison to the basic closure relations for FS emission

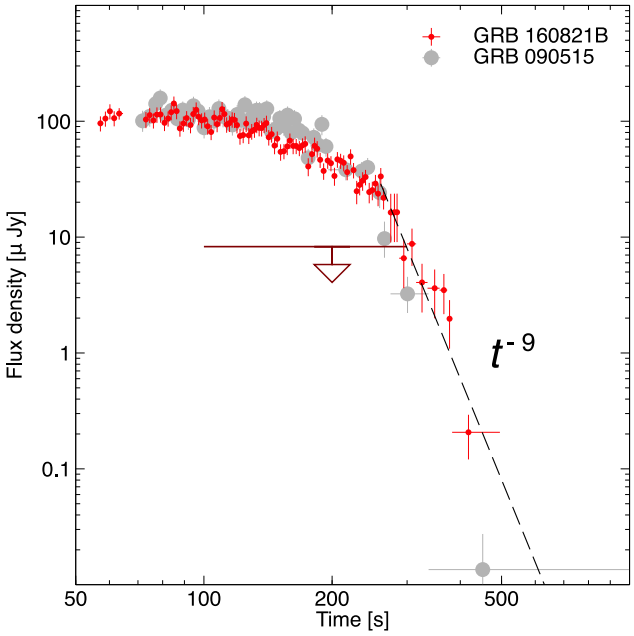

Figure 3. Temporal evolution of the early X-ray afterglow of GRB160821B (red circles) and, for comparison, GRB090515 (gray circles; Rowlinson et al. 2010). The sharp drop in flux ($\propto t^{-9}$, dashed line) and the deep upper limit from *Swift*/UVOT rule out an external shock origin for the observed X-ray emission.

(Zhang & Mészáros 2004) shows that the temporal slope α_1 is shallower than the predicted value $3\beta/2 \approx 1.05$. We interpret this flattening of the light curve as a viewing angle effect (e.g. Ryan et al. 2015) due to the contribution from the jet lateral structure. For this reason, we adopt a Gaussian jet profile, as described in Troja et al. (2017) and Troja et al. (2018a), to better model the afterglow evolution.

XMM-Newton data rule out the presence of an early ($\lesssim$1 d) temporal break, proposed by Jin et al. (2018) based on a smaller dataset. They are instead consistent with an uninterrupted power-law decay up to $\approx$4 d (3.5 d rest-frame) and no spectral evolution. The measured spectral index is $\beta = \Gamma - 1 = 0.88 \pm 0.24$, consistent with the earlier XRT spectrum. In the second epoch of XMM observations, the measured flux is three times lower than the predictions based on the simple power-law temporal decay. The lower flux is consistent with a steeper power-law decline of slope $\alpha_2 \sim 2.3$, and may indicate that a temporal break, likely a "jet-break" (Rhoads 1999; Sari et al. 1999), indeed occurred after 3.5 d.

Radio observations show a fading afterglow since early times. For standard FS emission, this may indicate that ν_m is already below the radio range and that radio, optical, and X-rays belong to the same spectral segment, as observed for GW170817 (D'Avanzo et al. 2018; Lyman et al. 2018; Troja et al. 2019). However, for GRB160821B the flat radio-to-optical spectral index $\beta_{OR} \approx 0.3$ at 4 hr rules out such regime, and shows that $\nu_m^{FS} \gg 6$ GHz. In this case, the fading radio light curve could be explained by an early jet-break (e.g. GRB140903A; Troja et al. 2016), a flaring episode (e.g. GRB050724A; Berger et al. 2005), or a RS component from the shock-heated relativistic ejecta (e.g. GRB051221A; Soderberg et al. 2006). Simultaneous X-ray data allow us to exclude the first two options, favoring the RS scenario. For a short GRB with $T_{90} \approx 0.5$ s, the more likely scenario is the thin-shell case leading to a Newtonian RS (Lloyd-Ronning 2018; Becerra et al. 2019). The early radio observations constrain the RS peak flux $F_{pk}^{RS} \gtrsim 26$ μJy and frequency $\nu_{pk}^{RS} \lesssim 6$ GHz at 3.5 hrs. Given the predicted evolution of the RS characteristic frequency $\nu_m^{RS} \propto t^{-1.5}$ (Kobayashi 2000), the RS peak was well below the optical range at 100 s, and therefore did not contribute to the early X-ray emission. Optical upper limits, down to $wh \gtrsim 21$ mag at $\approx$100 s (Figure 3), also exclude the presence of a bright RS component at early times.

Radio observations at later times help constrain the FS peak flux, $F_{pk}^{FS} \lesssim 50$ μJy, and synchrotron frequency, $\nu_{pk}^{RS} \gtrsim 100$ GHz at 1 d. For a homogeneous circumburst medium, the radio flux should rise as $t^{1/3}$, and eventually become visible at late times. The lack of detection at 10 d and 17 d therefore supports the presence of an earlier jet-break.

When viewed within the effective core opening angle θ_{core}, that is the viewing angle $\theta_{view} \lesssim \theta_{core}$, the afterglow of a FS with lateral structure is similar to that of a top hat jet viewed on-axis and the jet break time scales roughly as $\theta_{core}^{8/3}$, with deviations as θ_{view} approaches θ_{core} (Rossi et al. 2002). Numerical simulations of initially top-hat jets show that the observed jet-break time scales with these angles as $t_j = 3.5 \text{ d} \times (1+z) E_{50}^{1/3} n_{-3}^{-1/3} ((\theta_{core} + \theta_{view})/0.2)^{8/3}$, where E_{50} is the on-axis isotropic equivalent energy in units of 10^{50} erg and n_{-3} is the circumburst medium number density in units of 10^{-3} cm^{-3} (van Eerten et al. 2010). Then, using fiducial values $E_{50} = 1$ and $n_{-3} = 1$, the observed break in the light curve is consistent with a jet break if $\theta_{core} + \theta_{view} \approx 0.2$ rad.

3.2 Broadband Afterglow Modeling

Based on the preliminary constraints discussed in Sect. 3.1, we described the afterglow emission using a standard FS model and a structured jet with a Gaussian profile of width θ_{core}. We included in the fit the X-ray data, the late radio upper limits, and the first epoch of GTC optical/nIR observations ($\approx T_0 + 0.08$ d). The rest of the optical/nIR data (from $T_0 + 1$ d to $T_0 + 10.5$ d; Table 1) were treated as upper limits to the afterglow flux. The early radio detection, dominated by RS emission, was also not included.

Prior to the fit all the data were corrected for Galactic extinction. Given the evidence for negligible intrinsic absorption in the X-ray spectra, and also considered the GRB location in the outskirts of its host galaxy, we assumed $A_V^{host} \approx 0$. A small amount of extinction may affect our estimates of the spectral slope, but not the evident color evolution (Figure 2).

We followed the same procedure used in Troja et al. (2018a) and Troja et al. (2019), and performed a Bayesian Markov-Chain Monte Carlo (MCMC) model fit to data from synthetic detections generated from our jet model. Despite the large number of free parameters, the FS properties are reasonably well constrained:

$$\begin{aligned} \log E_{0,\rm iso}\ (\rm erg) &= 50.4\ (-0.3, +0.7) \\ \log n\ (\rm cm^{-3}) &= -2.8\ (-1.4, +1.1) \\ \log \epsilon_e &= -0.17\ (-0.22, +0.12) \\ \log \epsilon_B &= -2.1\ (-1.0, +1.0) \\ p &= 2.31\ (-0.05, +0.08) \end{aligned}$$

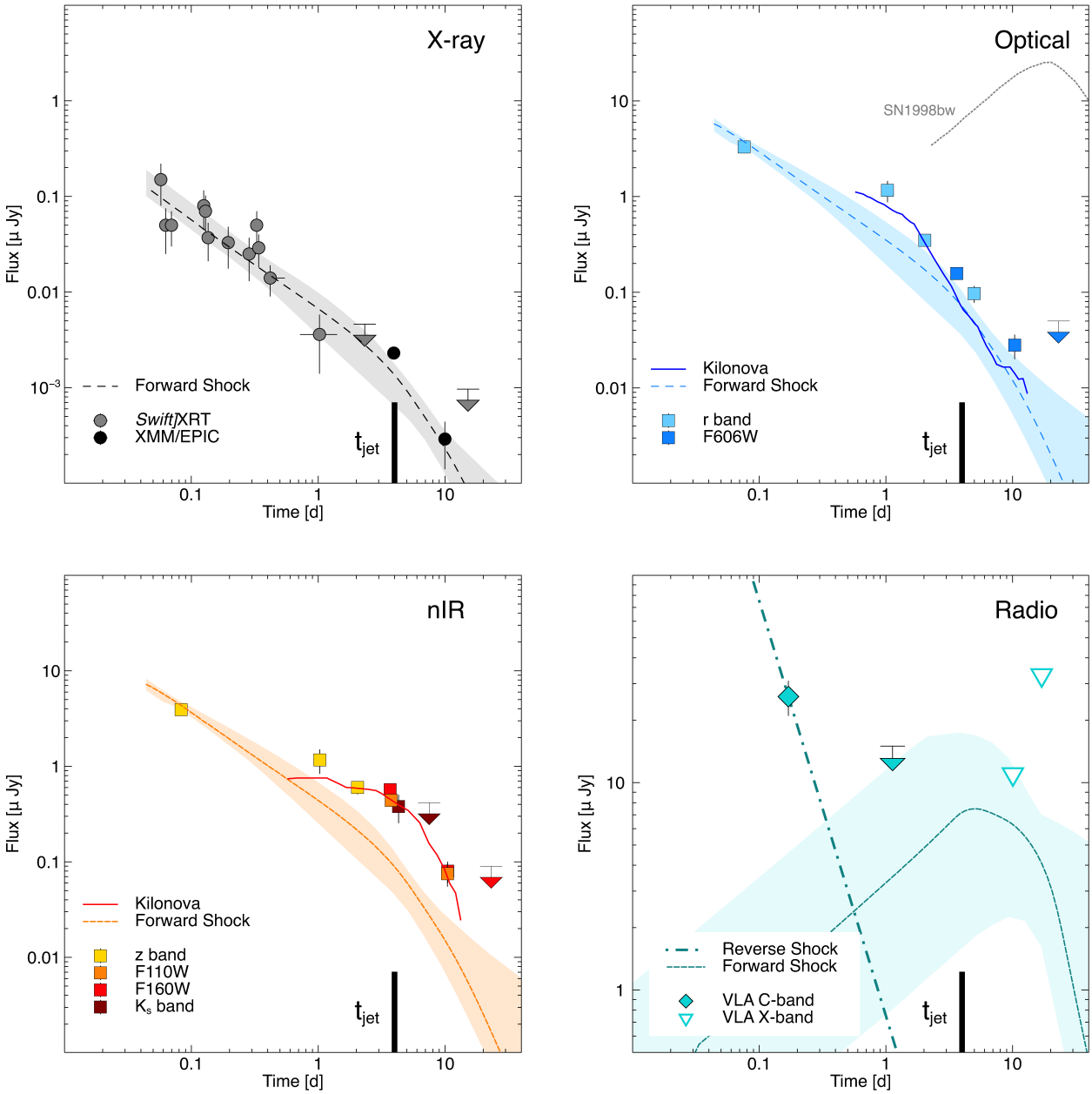

Figure 4. Multi-color lightcurves of GRB160821B compared to the standard FS (dashed line) + RS (dot-dashed line) scenario. The FS model is the best fit to the broadband dataset, whereas the RS is described as a fast fading power-law of slope ≈2 (Kobayashi 2000). The jet-break time $t_{\rm jet}$ is shown by the thick vertical line. The shaded areas show the 68% unceertainty in the model. Excess emission at optical and nIR wavelengths is compared with the template kilonova light curves of AT2017gfo (solid line). The redshifted optical light curve of SN1998bw (dotted line; Galama et al. 1998) is also shown for comparison. Errors are $1\,\sigma$, downward triangles are $3\,\sigma$ upper limits. For plotting purposes, r, z and K_s data were rescaled using the observed colors (Fig. 2) in order to match the F606W and F110W filters, respectively.

$$\theta_{core}\ (\rm rad) \;=\; 0.14\ (-0.06, +0.36)$$
$$\theta_{view}\ (\rm rad) \;=\; 0.17\ (-0.08, +0.25)$$

where $E_{0,\rm iso}$ is the isotropic equivalent blastwave energy, n the ambient density, ϵ_e and ϵ_B the shock microphysical parameters, and θ_{view} the observer's angle with respect to the jet-axis. The resulting prompt radiative efficiency is $\eta_\gamma = E_{\gamma,\rm iso}/\left(E_{\gamma,\rm iso}+E_{0,\rm iso}\right) = 0.05^{+0.05}_{-0.04}$. Viewing angle effects are taken into account into our modeling and the derived $E_{0,\rm iso}$, but not in the observed $E_{\gamma,\rm iso}$. Accounting for them would increase its value by a factor ≈3, that is $\eta_\gamma \approx 0.15$.

Our best fit model and its uncertainty are shown in Figure 4. In this model early emission at $T_0+0.1$ d is dominated by a small patch around the line of sight with Lorentz factor ~ 8. The patch widens as the jet decelerates, through the jet break, until at $T_0 + 10$d whole jet is in sight and has a Lorentz factor of roughly 1.5. Whereas at early times ($< T_0+0.1$ d) it provides a good representation of the broadband dataset, at later times it does not naturally account for the drastic color change of the optical/nIR data. It there-

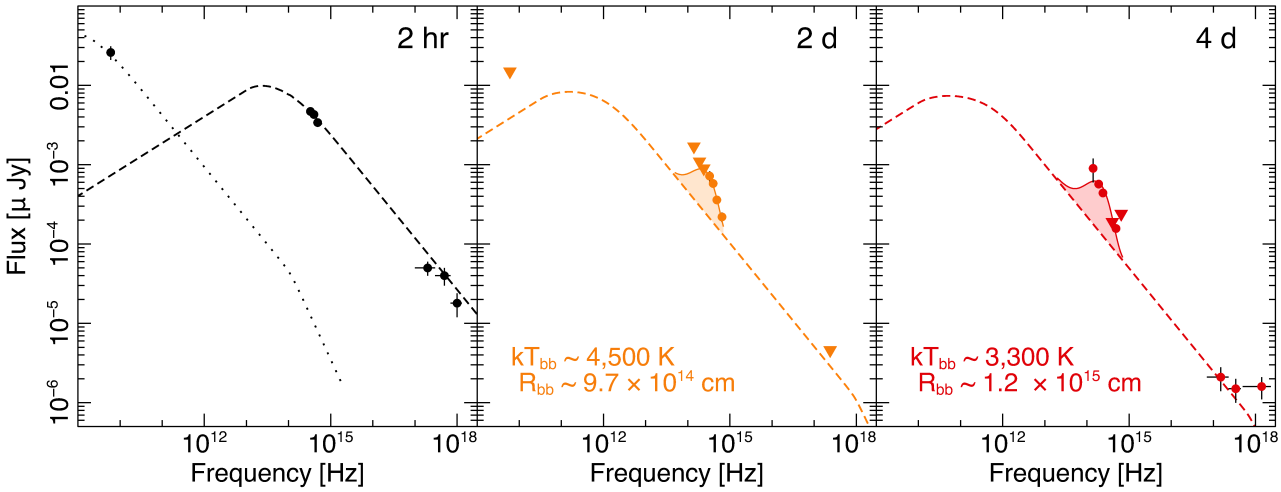

Figure 5. Broadband spectral energy distribution of GRB160821B. Downward triangles are 3 σ upper limits. A standard non-thermal afterglow, including a forward shock (dashed line) and a reverse shock (dotted line) component, can reproduce the early data (T_0+2 hr). At later times, an additional emission component is visible in the optical/nIR range. It can be described by a black-body spectrum (solid line) with decreasing temperature.

fore underpredicts the observed emission at nIR and, to a less extent, optical wavelengths. In Figure 4 we also overplot the template light curves for AT2017gfo in the $F606W$ and $F110W$ filters, rescaled to match the observed fluxes. The close resemblance between the temporal evolution of the optical /nIR excesses and the kilonova light curves suggests that they share a common origin.

Figure 5 reports the spectral energy distribution at three different epochs. Whereas at early times (T_0+2 hr) the broadband spectrum can be described by an afterglow model, at later times emission at optical/nIR wavelengths is brighter and redder than the model predictions (dashed line). This excess can be modeled with a black-body spectrum of decreasing temperature, from ≈4,500 K at 2 d to ≈3,300 K at 4 d, and radius $R \approx 10^{15}$ cm.

4 KILONOVA PROPERTIES

4.1 Comparison to AT2017gfo and GRB130603B

We interpret the red excess detected in GRB160821B as kilonova emission from fast-moving lanthanide-rich ejecta. This is only the second case of a short GRB with a kilonova detection in the nIR, where the emission is determined by the heaviest elements ($A \gtrsim 140$). In Figure 6, we compare its properties to the kilonova AT2017gfo and to the other candidate kilonova in GRB130603B. The IR emission of GRB130603B is brighter and longer lived, and its properties are not a good match, as reported in our preliminary analysis of this event (Troja et al. 2016). The observed emission resembles more closely the color and temporal evolution of AT2017gfo, although less luminous by ≈1 mag. Our results are consistent with the conclusions of Jin et al. (2018), and provide a better temporal and spectral coverage of the candidate kilonova.

The complexity of these systems, in particular the poorly known nuclear physics involved, lead to large uncertainties in the modeling of kilonovae light curves and spectra (e.g. Rosswog et al. 2017). We do not attempt here a systematic comparison to the various models presented in the literature, but estimate the basic explosion parameters based on the scaling relations of Grossman et al. (2014). The observed nIR luminosity, $L_{\rm nIR} \approx 2 \times 10^{39}$ erg s^{-1}, and timescales, $t_{\rm pk} \lesssim 3$ d, imply a low ejecta mass $M_{ej} \lesssim 0.006\ M_\odot$ and high velocity $v_{ej} \gtrsim 0.05c$ for an opacity $\kappa \approx 10$ g cm^{-3}. This result agrees well with the constraints $v \approx R_{bb}/t \approx 0.1\text{-}0.2\,c$, derived from simple black body fits (Figure 5). The ejecta mass is substantially lower than the values inferred for other GRB kilonovae (Jin et al. 2016; Yang et al. 2015; Tanvir et al. 2013), and comfortably within the range of dynamical ejecta from double NS mergers.

Our analysis also finds evidence for an early blue excess, although with larger uncertainties. It is suggestive that the luminosity and timescale of this blue component are consistent with the early optical emission in AT2017gfo (Figure 4, top right panel). The blue color and early onset require a larger mass ($M_{ej} \approx 0.01\ M_\odot$) of lanthanide-poor material, produced, for example, by the merger remnant.

4.2 Effects of a long-lived NS

The merger of two NSs can lead either to a stellar-mass BH or to a hypermassive highly magnetized NS (Giacomazzo & Perna 2013; Piro et al. 2017). The latter is thought to significantly affect both the kilonova colors and the afterglow evolution through its continuous energy injection and strong neutrino irradiation (Kasen et al. 2015; Gao et al. 2015; Lippuner et al. 2017; Radice et al. 2018). Indeed, the red colors of GW170817/AT2017gfo and its smooth afterglow light curve, mostly consistent with a standard FS emission, were used to exclude a wide range of possible NS configurations (Margalit & Metzger 2017; Ai et al. 2018). Only a short-lived proto-magnetar or a long-lived NS with a weak poloidal field could be consistent with the electromagnetic properties of GW170817 (Li et al. 2018; Metzger et al. 2018; Yu et al. 2018; Piro et al. 2019).

GRB160821B allows us to study the link between the

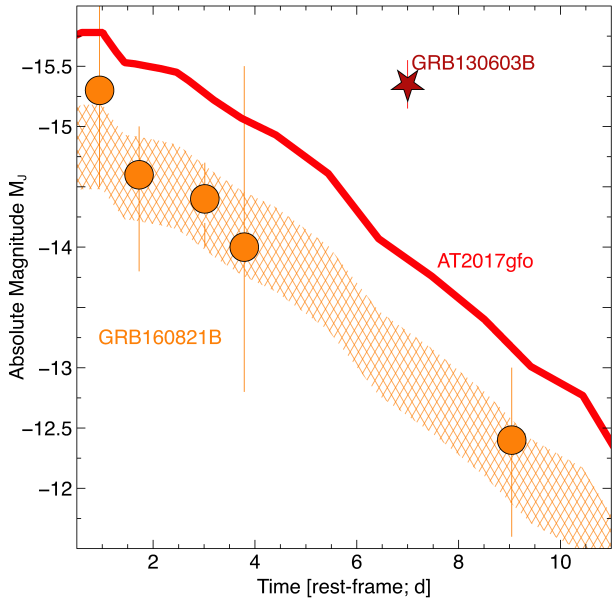

Figure 6. Rest-frame nIR light curves for AT2017gfo (red solid line) and the two candidate kilonovae in GRB 130603B (star) and GRB 160821B (circles). Error bars are $1\,\sigma$ statistical uncertainties. The hatched area shows the uncertainty in the afterglow subtraction.

GRB central engine and the kilonova properties. Its X-ray afterglow shows evidence of a long-lasting engine activity. In particular, the early X-ray emission shows a phase of nearly constant flux followed by a sharp decay (Figure 3) often interpreted as a signature of a proto-magnetar (Fan & Xu 2006; Troja et al. 2007; Liang et al. 2007; Lyons et al. 2010; Rowlinson et al. 2010; Dall'Osso et al. 2011). The sudden cessation of X-ray emission at $t \approx 200$ s may be caused by the NS collapse into a BH (Troja et al. 2007).

Within this framework, the observed plateau luminosity, $L_X \approx 5{\times}10^{47}$ erg s^{-1}, and its lifetime, $T \approx 200$ s, can be used to infer the magnetar properties (Zhang & Mészáros 2001). For an isotropic emission, Lü et al., (2017) derived an initial spin period $P_0 \approx 9$ ms and a dipolar magnetic field $B_0 \approx 3{\times}10^{16}$ G, in overall agreement with the assumption of a magnetar which suffered from dominant energy loss via gravitational wave radiation (Fan, Wu & Wei 2013). Beaming would substantially affect these results, and yield unphysical values of magnetic field and period. This indicates that, if the power source of the early X-ray emission is a newborn spindown NS, then the magnetar-driven outflow is nearly isotropic, in agreement with the recent claim of magnetar-driven fast X-ray transients (Xue et al. 2019).

Prolonged irradiation from the NS remnant will affect the ejecta composition and velocity profile, resulting in a bluer and short-lived kilonova emission. However, the color evolution of GRB160821B supports the presence of a red kilonova evolving on timescales similar to AT2017gfo, although less luminous by a factor of ≈2–5. While the lower IR luminosity could be an effect of the long-lived NS, the red excess shows that, despite it, a good amount of lanthanide-rich material was formed and released into the ambient medium, e.g. by tidally stripped matter ejected before the merger (Korobkin et al. 2012).

5 ENVIRONMENT

Late-time *HST* observations (Table 1) place deep upper limits on any galaxy underlying the GRB position. Such faint host galaxies are rarely observed in short GRBs (e.g. Piranomonte, et al. 2008) and imply, at least, a moderately high redshift $z \gtrsim 1$. Similar distance scales are disfavored by the presence of a kilonova, for which luminosities $>>10^{43}$ erg would lead to implausible properties of the merger ejecta. We consider more natural to link GRB160821B with the nearby bright galaxy (Figure 1), whose spectrum and disturbed morphology are consistent with a star-forming spiral galaxy, possibly undergoing a merger phase. At the measured offset of 5.7″, the probability of a chance alignment between the GRB and the galaxy is ≈2%. However, we find that the overall galaxy properties suggest an environment typical of short GRBs, thus strenghtening the case for a physical association.

The galaxy's absolute B-band magnitude is $M_B \approx$ -19.9 AB, approximately $0.7L^*_B$ for a late-type galaxy (Type 3+4; Zucca et al. 2009), and its colors are consistent with those of an irregular galaxy (Fukugita et al. 1995). It is detected in the WISE bands with $W1(3.4\ \mu\text{m}) = 20.52{\pm}0.10$ and $W2(4.6\ \mu\text{m}) = 21.0 \pm 0.3$ AB mag, from which we estimate a stellar mass $\log\,(M/M_\odot) \approx 8.5$ (Wen et al. 2013), at the lower end of the short GRB distribution (Berger 2014).

We used standard emission line diagnostics to infer the average properties of the putative host. The prominent nebular emission lines are indicative of on-going star formation. The [OII] line luminosity gives a star formation rate SFR([O II]) $\gtrsim 1.5\,M_\odot\,\text{yr}^{-1}$ (Kennicutt 1998), consistent with the estimate SFR(FUV) $\approx 1.2\,M_\odot\,\text{yr}^{-1}$ derived from the UV luminosity $M_{w2} \approx$-18.5 AB mag (Hao et al. 2011). Line ratios, $\log$ ([OIII]/$H\beta$)≈0.4 and $\log$ ([OIII]/[OII])≈-0.1, are substantially lower than in long GRB host galaxies, and within the range of short GRB hosts (Levesque & Kewley 2007). The solution based on the R_{23} (Pagel et al. 1979) and O_{32} indicators is degenerate, and we can only constrain the upper metallicity branch (Kobulnicky & Kewley 2004), for which we find $12 + \log(\text{O/H}) \approx 8.7$, consistent with a solar metallicity (Asplund et al. 2009).

The projected physical offset is ≈16.4 kpc from the galaxy's center, at the higher end of the offset distribution for short GRBs (Troja et al. 2008; Fong & Berger 2013; Tunnicliffe et al. 2014). As only a small fraction of stars is expelled during galaxy interactions (e.g. Behroozi et al. 2013), the observed offset is likely the result of an intrinsic kick imparted to the progenitor upon birth. For a stellar age of ≈300 Myr and a velocity dispersion $v_{disp} \approx 120\,\text{km s}^{-1}$, a minimum kick velocity $v_{kick} \gtrsim 80\,\text{km s}^{-1}$ would be required to reproduce the observed distance. However, a more detailed treatment, accounting for the galaxy's potential as well as the possibility of multiple orbits around the galaxy, finds that natal kicks larger than $150\,\text{km s}^{-1}$ are needed to explain the large offsets of some short GRBs (Behroozi et al. 2014).

An alternative explanation for short GRBs with large offsets was discussed by Salvaterra et al. (2010), who investigated compact binaries dynamically formed in globular clusters. At the distance of the candidate host, *HST* upper limits can only exclude the presence of luminous cluster systems, such as those found in M87, but are otherwise unconstrain-

ing. The range of circumburst densities from afterglow modeling (Sect. 3.2) is also compatible with an origin in a globular cluster (Freire et al. 2001).

6 CONCLUSIONS

GRB160821B is a nearby ($z \sim 0.1613$) short GRB with bright X-ray, radio and optical/nIR counterparts. The X-ray emission shows evidence for continued energy injection from a long-lived central engine, active up to $\approx$200 s after the burst. At later times, the X-ray afterglow is consistent with standard forward shock emission, whereas the radio signal was likely dominated by a weak reverse shock. Optical/nIR observations show a clear evolution toward red colors, consistent with the onset of a lanthanide-rich kilonova similar to AT2017gfo. The identification of this additional component is challenging due to the contamination from the underlying bright afterglow, and required an uncommonly rich dataset to be disentangled. Within the sample of short GRBs, this is only the second kilonova detected in the nIR. Its low luminosity implies a low mass of lanthanide-rich ejecta, possibly as an effect of a long-lived NS remnant.

7 ACKNOWLEDGEMENTS

This work is dedicated to the memory of John K. Cannizzo, a friend and colleague with whom we shared many stimulating conversations about kilonovae and short GRBs.

We thank the anonymous referee for his/her insightful and constructive comments. We gratefully thank R. Clavero and S. Dichiara for assistance, B. Metzger and J. Barnes for help in the preliminary modeling. We acknowledge the use of public data from the Swift data archive. This work made use of data supplied by the UK Swift Science Data Centre at the University of Leicester. These results also made use of Lowell Observatory's Discovery Channel Telescope. Lowell operates the DCT in partnership with Boston University, Northern Arizona University, the University of Maryland, and the University of Toledo. Partial support of the DCT was provided by Discovery Communications. LMI was built by Lowell Observatory using funds from the National Science Foundation (AST-1005313). The work is partly based on the observations made with the Gran Telescopio Canarias (GTC), installed in the Spanish Observatorio del Roque de los Muchachos of the Instituto de Astrofisica de Canarias, in the island of La Palma.

ET acknowledges financial support provided by the National Aeronautics and Space Administration through HST-GO14357, HST-GO14087, HST-GO14607 and HST-GO14850 grants from the Space Telescope Science Institute, operated by the Association of Universities for Research in Astronomy, Incorporated. AJCT, YDH e IM acknowledge financial support from the State Agency for Research of the Spanish MCIU through the "Center of Excellence Severo Ochoa" award for the Instituto de Astrofísica de Andalucía (SEV-2017-0709). The development of CIRCE at GTC was supported by the University of Florida and the National Science Foundation (grant AST-0352664), in collaboration with IUCAA. RSR acknowledges support by Italian Space Agency (ASI) through the Contract n. 2015-046-R.0 and by AHEAD the European Union Horizon 2020 Programme under the AHEAD project (grant agreement n. 654215). YDH also acknowledges the support by the program of China Scholarships Council (CSC) under the Grant No.201406660015. JBG acknowledges the support of the Viera y Clavijo program funded by ACIISI and ULL. GN and AT acknowledge funding in the framework of the project ULTraS (ASI–INAF contract N. 2017-14-H.0). GR acknowledges the support of the University of Maryland through the Joint Space Science Institute Prize Postdoctoral Fellowship.

REFERENCES

Abbott, B. P., Abbott, R., Abbott, T. D., et al., 2017, Physical Review Letters, 118, 221101
Abbott, B. P., Abbott, R., Abbott, T. D., et al. 2017, ApJ, 848, L12
Ai, S., Gao, H., Dai, Z.-G., et al. 2018, ApJ, 860, 57
Arnaud, K. A. 1996, Astronomical Data Analysis Software and Systems V, 101, 17
Asplund, M., Grevesse, N., Sauval, A. J., & Scott, P. 2009, ARA&A, 47, 481
Baiotti, L., Giacomazzo, B., & Rezzolla, L. 2008, Phys. Rev. D, 78, 084033
Barnes, J., & Kasen, D., 2013, ApJ, 775, 18
Barthelmy, S. D., Barbier, L. M., Cummings, J. R., et al. 2005, Space Sci. Rev., 120, 143
Becerra, R. L., Dichiara, S., Watson, A. M., et al., 2019, preprint, arXiv 1904.05987
Behroozi, P. S., Loeb, A., & Wechsler, R. H. 2013, J. Cosmology Astropart. Phys., 6, 019
Behroozi, P. S., Ramirez-Ruiz, E., & Fryer, C. L. 2014, ApJ, 792, 123
Berger, E., Price, P. A., Cenko, S. B., et al. 2005, Nature, 438, 988
Berger, E. 2014, ARA&A, 52, 43
Bertin, E., Mellier, Y., Radovich, M., et al. 2002, Astronomical Data Analysis Software and Systems XI, 281, 228
Bertin, E. 2006, Astronomical Data Analysis Software and Systems XV, 351, 112
Blanton, M. R., & Roweis, S. 2007, AJ, 133, 734
Blinnikov, S. I., Novikov, I. D., Perevodchikova, T. V., & Polnarev, A. G. 1984, Soviet Astronomy Letters, 10, 177
Bloom, J. S., Prochaska, J. X., Pooley, D., et al. 2006, ApJ, 638, 354
Bucciantini, N., Metzger, B. D., Thompson, T. A., & Quataert, E. 2012, MNRAS, 419, 1537
Breeveld, A. A., Landsman, W., Holland, S. T., et al. 2011, American Institute of Physics Conference Series, 1358, 373
Breeveld, A. A., & Siegel, M. H. 2016, GRB Coordinates Network, Circular Service, No. 19839, #1 (2016), 19839, 1
Burrows, D. N., Hill, J. E., Nousek, J. A., et al. 2005, Space Sci. Rev., 120, 165
Cash, W. 1979, ApJ, 228, 939
Chambers K. C., et al., 2016, arXiv e-prints, arXiv:1612.05560
Covino S., et al., 2017, NatAs, 1, 791
Dall'Osso, S., Stratta, G., Guetta, D., et al. 2011, A&A, 526, A121
D'Avanzo P., et al., 2018, A&A, 613, L1
Drout, M. R., Piro, A. L., Shappee, B. J., et al., 2017, Science, 358, 1570
Eichler, D., Livio, M., Piran, T., & Schramm, D. N., 1989, Nature, 340, 126
Evans, P. A., Beardmore, A. P., Page, K. L., et al. 2009, MNRAS, 397, 1177

Evans, P. A., Cenko, S. B., Kennea, J. A., et al., 2017, Science, 358, 1565
Fan, Y.-Z., & Xu, D. 2006, MNRAS, 372, L19
Fan Y.-Z., Wu X.-F., Wei D.-M., 2013, PhRvD, 88, 067304
Fong, W., & Berger, E. 2013, ApJ, 776, 18
Fong, W., Alexander, K. D., & Laskar, T. 2016, GRB Coordinates Network, Circular Service, No. 19854, #1 (2016), 19854, 1
Foreman-Mackey D., Hogg D. W., Lang D., Goodman J., 2013, PASP, 125, 306
Freiburghaus, C., Rosswog, S., & Thielemann, F.-K., 1999, ApJL, 525, L121
Freire P. C., Kramer M., Lyne A. G., Camilo F., Manchester R. N., D'Amico N., 2001, ApJL, 557, L105
Fukugita, M., Shimasaku, K., & Ichikawa, T. 1995, PASP, 107, 945
Gabriel, C., Denby, M., Fyfe, D. J., et al. 2004, Astronomical Data Analysis Software and Systems (ADASS) XIII, 314, 759
Galama, T. J., Vreeswijk, P. M., van Paradijs, J., et al. 1998, Nature, 395, 670
Gao, H., Ding, X., Wu, X.-F., Dai, Z.-G., & Zhang, B. 2015, ApJ, 807, 163
Gehrels, N., Chincarini, G., Giommi, P., et al. 2004, ApJ, 611, 1005
Ghirlanda G., et al., 2019, Sci, 363, 968
Giacomazzo, B., & Perna, R., 2013, ApJL, 771, L26
Gompertz, B. P., Levan, A. J., Tanvir, N. R., et al., 2018, ApJ, 860, 62
Goodman, J., 1986, ApJL, 308, L47
Goriely, S., Bauswein, A., & Janka, H.-T. 2011, ApJ, 738, L32
Granot J., Sari R., 2002, ApJ, 568, 820
Green, G. M., Schlafly, E. F., Finkbeiner, D., et al. 2018, MNRAS, 478, 651
Grossman, D., Korobkin, O., Rosswog, S., & Piran, T. 2014, MNRAS, 439, 757
Hallinan G., et al., 2017, Science, 358, 1579
Hao C.-N., Kennicutt R. C., Johnson B. D., Calzetti D., Dale D. A., Moustakas J., 2011, ApJ, 741, 124
Hotokezaka, K., Kyutoku, K., Tanaka, M., et al., 2013, ApJL, 778, L16
Jin, Z.-P., Hotokezaka, K., Li, X., et al. 2016, Nature Communications, 7, 12898
Jin, Z.-P., Li, X., Wang, H., et al., 2018, ApJ, 857, 128
Kann, D. A., Klose, S., Zhang, B., et al., 2011, ApJ, 734, 96
Kasen, D., Fernández, R., & Metzger, B. D. 2015, MNRAS, 450, 1777
Kasen, D., Metzger, B., Barnes, J., Quataert, E., & Ramirez-Ruiz, E., 2017, Nature, 551, 80
Kasliwal, M. M., Korobkin, O., Lau, R. M., Wollaeger, R., & Fryer, C. L., 2017, ApJL, 843, L34
Kennicutt, R. C., Jr. 1998, ARA&A, 36, 189
Kobayashi, S. 2000, ApJ, 545, 807
Kobulnicky, H. A., & Kewley, L. J. 2004, ApJ, 617, 240
Kocevski, D., Thöne, C. C., Ramirez-Ruiz, E., et al. 2010, MNRAS, 404, 963
Korobkin, O., Rosswog, S., Arcones, A., & Winteler, C., 2012, MNRAS, 426, 1940
Kiuchi, K., Sekiguchi, Y., Shibata, M., & Taniguchi, K. 2009, Phys. Rev. D, 80, 064037
Lattimer, J. M., & Schramm, D. N., 1974, ApJL, 192, L145
Lattimer, J. M., & Schramm, D. N., 1976, ApJ, 210, 549
Lazzati D., Perna R., Morsony B. J., Lopez-Camara D., Cantiello M., Ciolfi R., Giacomazzo B., Workman J. C., 2018, [Physical Review Letters], 120, 241103
Levan, A. J., Wiersema, K., Tanvir, N. R., et al. 2016, GRB Coordinates Network, Circular Service, No. 19846, #1 (2016), 19846, 1
Levesque, E. M., & Kewley, L. J. 2007, ApJ, 667, L121
Li, L.-X., & Paczyński, B., 1998, ApJL, 507, L59
Li L., et al., 2018, ApJS, 234, 26
Li, S.-Z., Liu, L.-D., Yu, Y.-W., & Zhang, B. 2018, ApJ, 861, L12
Liang, E.-W., Zhang, B.-B., & Zhang, B. 2007, ApJ, 670, 565
Lien, A., Sakamoto, T., Barthelmy, S. D., et al. 2016, ApJ, 829, 7
Lippuner, J., Fernández, R., Roberts, L. F., et al. 2017, MNRAS, 472, 904
Lloyd-Ronning, N. 2018, Galaxies, 6, 103
Lyman J. D., et al., 2018, Nature Astronomy
Lyons, N., O'Brien, P. T., Zhang, B., et al. 2010, MNRAS, 402, 705
Lü H.-J., Zhang H.-M., Zhong S.-Q., Hou S.-J., Sun H., Rice J., Liang E.-W., 2017, ApJ, 835, 181
Margalit, B., & Metzger, B. D. 2017, ApJ, 850, L19
Melandri A., et al., 2017, A&A, 607, A29
Metzger, B. D., Martínez-Pinedo, G., Darbha, S., et al., 2010, MNRAS, 406, 2650
Metzger, B. D., Thompson, T. A., & Quataert, E. 2018, ApJ, 856, 101
Mooley K. P., et al., 2018, Nature, 554, 207
Narayan, R., Paczynski, B., & Piran, T., 1992, ApJL, 395, L83
Ofek, E. O., Cenko, S. B., Gal-Yam, A., et al., 2007, ApJ, 662, 1129
Oke, J. B. 1974, ApJS, 27, 21
Paczynski, B., 1986, ApJL, 308, L43
Pagel, B. E. J., Edmunds, M. G., Blackwell, D. E., Chun, M. S., & Smith, G. 1979, MNRAS, 189, 95
Pandey, S. B., Hu, Y., Castro-Tirado, A. J., et al. 2019, MNRAS, 485, 5294
Paschalidis V., Ruiz M., Shapiro S. L., 2015, ApJ, 806, L14
Perego, A., Radice, D., & Bernuzzi, S. 2017, ApJ, 850, L37
Perley, D. A., Metzger, B. D., Granot, J., et al., 2009, ApJ , 696, 1871
Pian, E., D'Avanzo, P., Benetti, S., et al., 2017, Nature, 551, 67
Piranomonte S., et al., 2008, A&A, 491, 183
Piro, A. L., Giacomazzo, B., & Perna, R., 2017, ApJL, 844, L19
Piro, L., Troja, E., Zhang, B., et al. 2019, MNRAS, 483, 1912
Planck Collaboration et al., 2018, preprint, arXiv 1807.06209
Radice, D., Perego, A., Hotokezaka, K., et al. 2018, ApJ, 869, 130
Rezzolla, L., Giacomazzo, B., Baiotti, L., et al., 2011, ApJL, 732, L6
Rhoads, J. E. 1999, ApJ, 525, 737
Ryan, G., van Eerten, H., MacFadyen, A., & Zhang, B.-B. 2015, ApJ, 799, 3
Roberts, L. F., Kasen, D., Lee, W. H., & Ramirez-Ruiz, E. 2011, ApJ, 736, L21
Roming P. W. A., et al., 2006, ApJ, 651, 985
Rossi E., Lazzati D., Rees M. J., 2002, MNRAS, 332, 945
Rossi, A., Stratta, G., Maiorano, E., et al. 2019, arXiv:1901.05792
Rosswog, S., Korobkin, O., Arcones, A., Thielemann, F.-K., & Piran, T. 2014, MNRAS, 439, 744
Rosswog, S., Feindt, U., Korobkin, O., et al. 2017, Classical and Quantum Gravity, 34, 104001
Rowlinson, A., O'Brien, P. T., Tanvir, N. R., et al. 2010, MNRAS, 409, 531
Ruffert, M., & Janka, H.-T. 1999, A&A, 344, 573
Ruiz, M., Lang, R. N., Paschalidis, V., & Shapiro, S. L. 2016, ApJ, 824, L6
Sari R., Piran T., Halpern J. P., 1999, ApJ, 519, L17
Salvaterra R., Devecchi B., Colpi M., D'Avanzo P., 2010, MNRAS, 406, 1248
Skrutskie, M. F., Cutri, R. M., Stiening, R., et al. 2006, AJ, 131, 1163
Soderberg, A. M., Berger, E., Kasliwal, M., et al., 2006, ApJ, 650, 261
Smartt, S. J., Chen, T.-W., Jerkstrand, A., et al., 2017, Nature, 551, 75
Strüder, L., Briel, U., Dennerl, K., et al. 2001, A&A, 365, L18

Tanaka, M., & Hotokezaka, K., 2013, ApJ, 775, 113
Tanaka, M., Hotokezaka, K., Kyutoku, K., et al., 2014, ApJ, 780, 31
Tanvir, N. R., Levan, A. J., Fruchter, A. S., et al. 2013, Nature, 500, 547
Tanvir, N. R., Levan, A. J., González-Fernández, C., et al., 2017, ApJL, 848, L27
Troja, E., Cusumano, G., O'Brien, P. T., et al. 2007, ApJ, 665, 599
Troja, E., King, A. R., O'Brien, P. T., Lyons, N., & Cusumano, G. 2008, MNRAS, 385, L10
Troja E., et al., 2016, ApJ, 827, 102
Troja, E., Tanvir, N., Cenko, S. B., et al. 2016, GRB Coordinates Network, Circular Service, No. 20222, #1 (2016), 20222, 1
Troja E., et al., 2017, Nature, 551, 71
Troja E., et al., 2018b, MNRAS, 478, L18
Troja, E., Ryan, G., Piro, L., et al. 2018, Nature Communications, 9, 4089
Troja, E., van Eerten, H., Ryan, G., et al. 2018, arXiv:1808.06617
Tunnicliffe, R. L., Levan, A. J., Tanvir, N. R., et al. 2014, MNRAS, 437, 1495
Turner, M. J. L., Abbey, A., Arnaud, M., et al. 2001, A&A, 365, L27
Uhm, Z. L., & Beloborodov, A. M. 2007, ApJ, 665, L93
Zucca, E., Bardelli, S., Bolzonella, M., et al. 2009, A&A, 508, 1217
van Eerten H., Zhang W., MacFadyen A., 2010, ApJ, 722, 235
van Eerten, H. 2014, MNRAS, 442, 3495
Wen, X.-Q., Wu, H., Zhu, Y.-N., et al. 2013, MNRAS, 433, 2946
Willingale, R., Starling, R. L. C., Beardmore, A. P., Tanvir, N. R., & O'Brien, P. T. 2013, MNRAS, 431, 394
Wollaeger, R. T., Korobkin, O., Fontes, C. J., et al. 2018, MNRAS, 478, 3298
Yang, B., Jin, Z.-P., Li, X., et al., 2015, Nature Communications, 6, 7323
Yu, Y.-W., Liu, L.-D., & Dai, Z.-G. 2018, ApJ, 861, 114
Xu D., Malesani D., de Ugarte Postigo A., Gafton E., Rivero Losada I., 2016, GCN, 19834, 1
Xue Y. Q., et al., 2019, Natur, 568, 198
Zhang, B., & Mészáros, P. 2001, ApJ, 552, L35
Zhang, B., & Mészáros, P. 2004, International Journal of Modern Physics A, 19, 2385